Comparison of FDTD Algorithms for Subcellular Modeling of Slots in Shielding Enclosures

Kuang-Ping Ma, Min Li, James L. Drewniak, *Member, IEEE*, Todd H. Hubing, *Senior Member, IEEE*, and Thomas P. Van Doren, *Senior Member, IEEE*

***Abstract*— Subcellular modeling of thin slots in the finite-difference time-domain (FDTD) method is investigated. Two subcellular algorithms for modeling thin slots with the FDTD method are compared for application to shielding enclosures in electromagnetic compatibility (EMC). The stability of the algorithms is investigated, and comparisons between the two methods for slots in planes, and slots in loaded cavities are made. Results for scattering from a finite-length slot in an infinite plane employing one of the algorithms are shown to agree well with published experimental results, and power delivered to an enclosure with a slot agree well with results measured for this study.**

***Index Terms*— FDTD, slot.**

I. Introduction

RADIATION from slots and seams in conducting enclosures is of greater concern in meeting FCC Class A and B limits as the speed of the electronic designs increases. The integrity of typical shielding enclosure designs is compromised by numerous slots and apertures for CD-ROM's, heat vents, and input/output (I/O) cables among others. Energy is coupled through these slots, and radiated to the external environment. Understanding the coupling mechanisms involving seams and coupling to nearby attached cables will therefore be important for estimating and reducing electromagnetic interference (EMI).

The finite-difference time-domain (FDTD) method has been widely applied in solving many types of electromagnetic scattering problems [1], [2]. It possesses the advantages of simple implementation for relatively complex problems, and high accuracy. A disadvantage of the FDTD method is that significant computational resources are expended for modeling an electrically small object without the aid of special subcellular or multigrid algorithms. Radiation from thin slots in enclosures, as well as coupling energy from external fields to the enclosures through a thin slot, fall into this category because the slot thickness can be much smaller than a desirable grid dimension. In addition to the increased memory required to fully discretize a thin slot, the run time is also increased by virtue of a smaller time-step to satisfy the Courant–Friedrichs–Lewy (CFL) stability criterion. Several subcellular thin-slot formalisms (TSF) have been proposed to circumvent the need for fully gridding a thin slot [3], [4]. Utilizing these TSF's, a thin slot segment can be modeled with a single cell, thereby saving computational resources while retaining accuracy. Subcellular FDTD thin-slot algorithms are considered in this paper. Two subcellular TSF algorithms developed by Gilbert and Holland [capacitance-thin-slot formalisms (C-TSF)] [3], and Riley and Turner [hybrid thin-slot algorithm (HTSA)] [4], are briefly summarized. Results comparing these two TSF's for plane-wave scattering from three-dimensional (3-D) finite plates, and loaded cavities are presented. The C-TSF algorithm proposed by Gilbert and Holland is employed to model a finite-length slot on an infinite plane, and the results are compared to published experimental results. The two subcellular algorithms are also compared to measured results for power delivered to an enclosure with a slot. Stability for these two TSF's is also investigated.

Manuscript received May 25, 1995; revised February 11, 1997.

The authors are with the Electromagnetic Compatibility Laboratory, Department of Electrical Engineering, University of Missouri, Rolla, MO 65409 USA.

Publisher Item Identifier S 0018-9375(97)03690-9.

II. FDTD Modeling and Thin-Slot Subcellular Algorithms

The FDTD method has been used extensively for solving many electromagnetic scattering problems since its introduction by Yee in 1966. A general discussion of the FDTD method including finite-difference equations for updating the fields, domain discretization, numerical dispersion, absorbing boundary conditions, and stability criterion, are readily available in the literature [1], [2].

Uniform plane-wave scattering from slots in finite and infinite conducting geometries are of interest in this study. The incident plane-wave source at infinity must be introduced into the FDTD algorithm without interfering with the scattered field. Several methods for implementing an incident plane wave in the FDTD method are given in the literature [1].

The computational domain must be truncated with absorbing boundary conditions (ABC's). While several ABC's have been proposed during the last decade, second-order Mur [5], and Liao [6], and perfectly matched layer (PML) ABC's [7] are used in this study. Second-order Mur absorbing boundary conditions are among the most frequently cited, and work well in many cases. For one of the cases in this investigation, it is necessary to place the absorbing boundaries close to the scatterer because of limited computational resources. Liao ABC's are employed in this situation. Due to the inherent instability, Liao ABC's are used with double-precision arithmetic, although memory requirements are significantly increased. A modified form of Liao ABC's requires only single-precision arithmetic [8], however, the parameters for the modified Liao ABC's are found to be machine-dependent. To

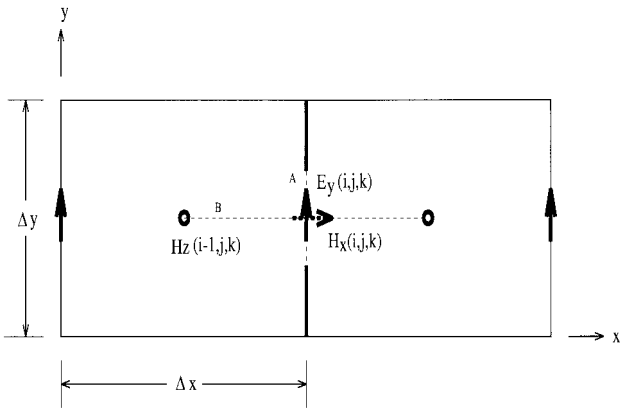

Fig. 1. FDTD cells around the slot for the C-TSF subcellular algorithm.

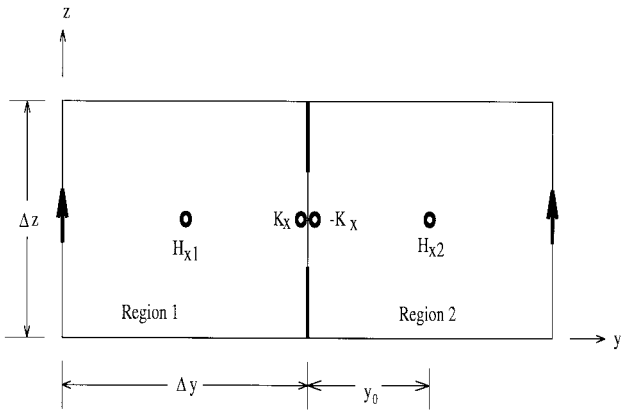

Fig. 2. FDTD cells around the slot for the HTSA method. The plate is shorted. The electric fields inside the slot are set to zero, and replaced by equivalent magnetic currents on either side of the plane.

ensure maximum stability throughout the simulations without determining optimal parameters for a modified Liao ABC, double-precision arithmetic and a small amount of loss are employed in this study, unless otherwise specified.

There are several choices for plane-wave source implementation and ABC's. The best choice is often case-dependent. For simulating 3-D finite objects, a total-field/scattered-field formulation with Mur ABC's is used, while for 3-D infinite objects, a scattered-field formulation with modified Liao ABC's is employed.

Two different subcellular thin-slot algorithms are employed for modeling thin slots in enclosures and conducting plates. The first method introduced by Gilbert and Holland [3], denoted herein as the C-TSF, is based on a straight-forward quasi-static approximation. Two-dimensional (2-D) C-TSF results for plane-wave scattering from a slot in an infinite conducting plane have been shown to agree well with method of moments (MoM) results. Typical discrepancies of less than 10% can be expected for the field quantities at locations near but not in the slot region [9]. The Yee cells around a slot oriented along the $\hat{z}$-axis are shown in Fig. 1. Employing a quasi-static approximation for narrow slots, and assuming the field quantities vary slowly in the $\hat{z}$-direction, the slot can be viewed as a coplanar, parallel strip capacitor [3]. The slot is then modeled by modifying the relative permittivity and relative permeability in the FDTD algorithm for the electric and magnetic field components in the slot.

The FDTD C-TSF time-marching equations can be obtained for the electric field and magnetic field components in the slot by defining two line integrals, one transverse to the slot, and the other across the slot. These line integrals can be employed with the integral form of Maxwell's equations to obtain modified FDTD update equations for the field components in the slot [3]. An extra parameter results in the finite-difference equation which is the ratio of the two line integrals, and can be shown to be an effective permittivity for the slot [3]. The relative permittivity in the slot is then written as [3]

$$\begin{aligned}\epsilon_r &= \frac{1}{\epsilon_0}\frac{\Delta y}{\Delta x}\frac{Q}{V} \\ &= \frac{1}{\epsilon_0}\frac{\Delta y}{\Delta x}C \end{aligned} \tag{1}$$

where C is the parallel strip capacitance per unit length. The capacitance is evaluated within only one FDTD cell, and is denoted as the in-cell capacitance. In order to maintain the free-space phase velocity through the slot $c_0 = (\epsilon_r\mu_r\epsilon_0\mu_0)^{-1/2}$, the relative permeability in the slot is given by ($\mu_r = 1/\epsilon_r$). Therefore, the electric and magnetic field components in the slot can be updated by modifying only the permittivity and permeability in the respective equations as

$$\begin{aligned}\tilde{E}^{n+1}_{y_{i,j,k}} &= \tilde{E}^{n}_{y_{i,j,k}} + \frac{\Delta t}{\epsilon_r\epsilon_0\Delta z}\left(\tilde{H}^{n+1/2}_{x_{i,j,k}} - \tilde{H}^{n+1/2}_{x_{i,j,k-1}}\right) \\ &\quad - \frac{\Delta t}{\epsilon_r\epsilon_0\Delta x}\left(H^{n+1/2}_{z_{i,j,k}} - H^{n+1/2}_{z_{i-1,j,k}}\right) \end{aligned} \tag{2}$$

$$\begin{aligned}\tilde{H}^{n+1/2}_{x_{i,j,k}} &= \tilde{H}^{n-1/2}_{x_{i,j,k}} + \frac{\Delta t}{\mu_r\mu_0\Delta z}\left(\tilde{E}^{n}_{y_{i,j,k+1}} - \tilde{E}^{n}_{y_{i,j,k}}\right) \\ &\quad - \frac{\Delta t}{\mu_r\mu_0\Delta y}\left(E^{n}_{z_{i,j+1,k}} - E^{n}_{z_{i,j,k}}\right) \end{aligned} \tag{3}$$

for the slot shown in Fig. 1. The tilde terms are the average values in and across the slot for the electric and magnetic field components, respectively. The slot capacitance per unit length is [9]

$$C_{in-cell} = \frac{\epsilon_0 K\left[\sqrt{1-\dfrac{w_s^2}{\Delta y^2}}\right]}{k\left(\dfrac{w_s}{\Delta y}\right)} \tag{4}$$

where $K()$ is the complete elliptic integral of the first kind, and w_s is the slot width. The relative pemittivity is then related to the slot capacitance by (1).

The integral-equation based HTSA is a more sophisticated thin-slot algorithm, but is also more complicated to implement [4]. The HTSA is based on an integro-differential equation in the frequency domain developed for electromagnetic scattering from arbitrary slots and apertures in infinite conducting planes [10]. A section of a perfect electric conducting plate with a slot, embedded in a Yee mesh, is shown in Fig. 2. An equivalent problem is developed by shorting the plate and replacing the slot by an equivalent antenna with radius $w_s/4$ for an infinitely thin plate. Then, a time-domain integro-differential equation relating the magnetic current of the equiv-

alent antenna to the short-circuit magnetic fields on either side of the slot is [4]

$$\mu_0 \frac{\partial (H_x^{sc_2} - H_x^{sc_1})}{\partial t} = 2\left(\frac{\partial^2}{\partial x^2} - \frac{1}{c^2}\frac{\partial^2}{\partial t^2}\right) \int_{-L_s/2}^{L_s/2} \cdot \frac{K_x\left(x'; t - \frac{R_a}{c}\right)}{2\pi R_a} dx' \quad (5)$$

where $R_a = \sqrt{a^2 + (x - x')^2}$, $H_x^{sc_{1,2}}$ are the short-circuit fields in Regions 1 and 2, respectively, and a is the equivalent antenna radius. The short-circuit magnetic field in Region 1 for example is the total field obtained in Region 1 as a result of an incident field scattered from the shorted conducting plane. The total magnetic current K_x is $K_x(x; t) = \int_{-w_s/2}^{w_s/2} dz\, M_x(x, z; t)$; where $\hat{x}M_x = \hat{y} \times \hat{z}E_a$, M_x is the magnetic current density, and E_a is the electric field in the aperture prior to shorting the conducting plane. This equation is derived based on image theory, and is strictly valid only for infinite planar conducting plates. However, results presented in this paper indicate that it works well even for slots in conducting rectangular enclosures. Equation (5) can be discretized by expanding the magnetic current with pulse basis functions in both space and time, then employing central differences for all differential operators. An explicit finite-difference equation for time-marching the magnetic current results [4]. The slot is accounted for by appending the magnetic current to the regular finite difference updating equation as

$$H_{x_{1,2}}^{n+1/2} = H_{x_{1,2}}^{n-1/2} - \frac{\Delta t}{\mu_0}(\nabla \times \overline{E}^n)_{x_{1,2}} \pm \frac{\Delta t}{\mu_0}\frac{1}{\Delta y}\frac{w_s}{\Delta z}\frac{1}{w_s} K_i^n \quad (6)$$

where the plus sign is for Region 2, and the minus sign is for Region 1 as shown in Fig. 2. In this manner, the radiation from the magnetic current can be incorporated into the FDTD calculations. It should be noted that the $\hat{z}$-component of the electric field in the slot is set to zero, and the slot is completely accounted for in the FDTD algorithm by an equivalent magnetic current. This current affects the update equations for only those magnetic-field components parallel and adjacent (by one-half cell) to the slot as shown in Fig. 2. One advantage of the HTSA over the C-TSF is the ability to model finite thickness slots through the equivalent antenna radius [11].

III. Numerical Results

The C-TSF and HTSA subcellular algorithms are implemented with the FDTD method, and numerical results are presented for 3-D finite plates, 3-D loaded cavities, and a 3-D infinite perfect electric conducting (pec) plane with a finite-length slot. All pec walls have zero thickness. Two excitations are used.

1) Gaussian pulse.
2) Electromagnetic pulse (EMP) [12].

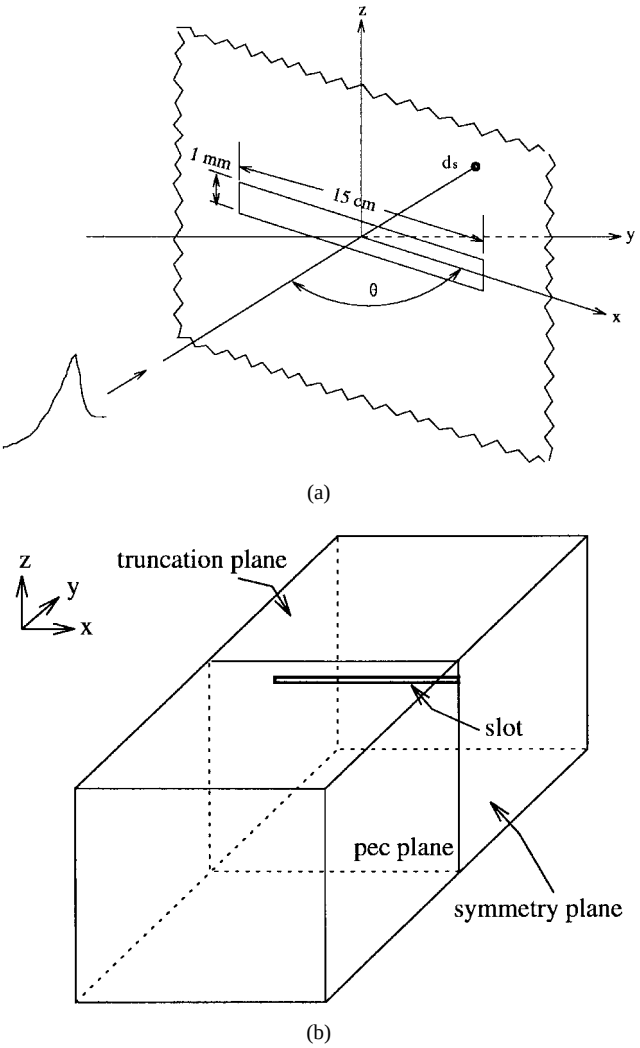

Fig. 3. The geometry of the 3-D infinite conducting plane and the computational domain: (a) geometry, and b) computational domain.

Time-domain responses are converted to frequency-domain responses using a fast Fourier transform (FFT).

First, scattering from a finite-length slot in a 3-D infinite pec plane is studied using the C-TSF and HTSA algorithms to model the slot. This problem is important because MoM, time-domain MoM, and experimental results are available in the literature for comparison [12]. The geometry of the plate, shown in Fig. 3(a), is that employed by Reed and Butler [12]. The ratio of the slot width to length is $w_s/L_s \approx 0.007$. Both C-TSF and HTSA are used to model the slot. For the C-TSF, the relative permittivity is calculated using the coplanar strip capacitance for the "in-cell" capacitance [9]. For this case, $\epsilon_r = 2.018$, corresponding to $w_s = 1$ mm, and $\mu_r = 1/\epsilon_r$. A scattered-field formulation and Liao ABC's are used. Double-precision arithmetic is employed to avoid the inherent instability of the Liao ABC's. Symmetry is exploited to reduce the memory requirements for the problem. Fig. 3(b) shows the computational domain when symmetry conditions are applied. One symmetry plane and one truncation plane are chosen to reduce the computational domain to approximately 1/4 of the original size. The truncation plane exploits symmetry along the direction perpendicular to the slot, and the symmetry plane

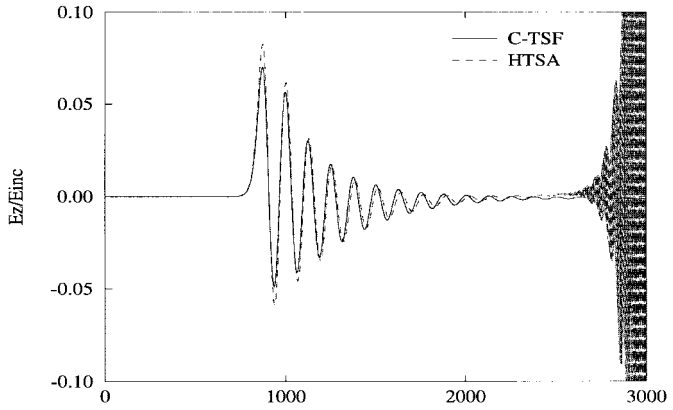

Fig. 4. Time-domain responses of a finite-length slot excited by an EM pulse.

exploits symmetry along the slot axis. However, since the slot must be included, the truncation plane is not a symmetry plane. Cubic FDTD cells, 0.5 cm on a side are used. The total mesh dimensions are 36 × 44 × 23 cells in the $\hat{x}$, $\hat{y}$, and $\hat{z}$ directions, respectively. The infinite pec plane is illuminated by a normally incident, $\hat{z}$-polarized electromagnetic pulse of the form [12]

$$E_z^{inc}(t) = \frac{1}{0.8258}\,\frac{1}{e^{-20[(t-t_0)/\beta]} + e^{(t-t_0)/\beta}} \tag{7}$$

where $t_0 = 6.67 \times 10^{-9}$ s and $\beta = 3.251 \times 10^{-9}$ s. The time step is 8.339 ps, and the time delay t_0 is such that the pulse starts with approximately zero amplitude. For the HTSA, the equivalent antenna radius is $w_s/4 = 0.25$ mm. Fig. 4 shows the comparison of the time domain responses for the C-TSF and HTSA methods for E_z at a point 5 cm away from the slot on the shadow side of the plane along the $\hat{y}$-axis. A late-time instability occurs for the HTSA method in this particular case, while by contrast, the C-TSF algorithm is stable. The periodicity of the ringing is approximately 1.02 ns and results from the half-wavelength resonance of the 15 cm slot. There is a slight time shift between the HTSA and C-TSF results that occurs as a result of the fundamental differences in formulation. Extensive comparison with experimental results have shown that for lower Q resonances ($Q < 20$), HTSA results agree well with measurements, however, there is a slight shift to higher frequency for the C-TSF results. Typically the shift is less than 1% depending on the Q [13]. For high-Q resonances, the agreement of both with measurements is good.

Experimental results for scattering from a finite-length slot in an "infinite" plane are available in the literature [12]. Only the C-TSF algorithm is compared with experimental results because of the late-time instability of the HTSA. The geometry of the slot is the same as that of the previous case. Cubic FDTD cells, 0.25 cm on a side are used for better high frequency resolution, and the total mesh dimensions are (51 × 54 × 23) cells in the $\hat{x}$, $\hat{y}$, and $\hat{z}$ directions, respectively. The infinite pec plane is illuminated by a normally incident, $\hat{z}$-polarized, sinusoidally modulated electromagnetic pulse of the form

$$E_z^{inc}(t) = \frac{1}{0.8258}\,\frac{1}{e^{-20[(t-t_0)/\beta]} + e^{(t-t_0)/\beta}} \cdot \cos\left[2\pi(f - f_s)t\right] \tag{8}$$

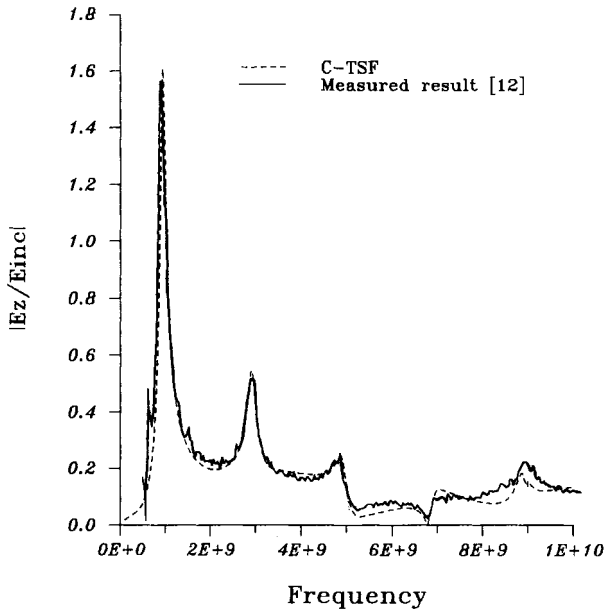

Fig. 5. Comparison between experimental results and the results for a finite-length slot in an infinite conducting plane modeled by C-TSF for a normally incident plane wave.

where f_s can be adjusted to shift the center frequency of the excitation. The time step is 4.169 ps. The slot length is 15 cm, and the slot width for this case is 1 mm. The FDTD cell size is reduced to half of that for the previous case, so the corresponding ϵ_r is 1.4983. The other parameters are the same as those of the previous case, and a scattered-field formulation with modified Liao ABC's is used. A moderately narrow-band EM pulse is employed, and several executions with increasing f_s are run to obtain the frequency response up to 10 GHz. Fig. 5 shows the comparison between FDTD results and published measured results [12]. The comparison is good up to approximately 5 GHz. Since the FDTD cells being used are 0.25 cm, the frequency at which $\Delta/\lambda = \frac{1}{24}$ is 5 GHz. Above 5 GHz the discretization becomes coarse, and discrepancies result. C-TSF results are compared with published results in Fig. 6 for the same problem, with the uniform plane-wave excitation incident at $\theta = 60°$, where θ is the angle from the $\hat{x}$-axis. The agreement is good up to 3 GHz, however, from 3–10 GHz there are discrepancies. While the FDTD simulations agree well with the resonance at 5 GHz, from 3–5 GHz, the agreement is not as good as for normal incidence in this frequency range. There are several possibilities for the difference in agreement for the two cases. The in-cell capacitance for the C-TSF method could possibly be somewhat dependent on incident angle. FDTD numerical grid dispersion could contribute, and measurement error may be a factor.

A thin slot in a finite plate with dimensions shown in Fig. 7 is also modeled. Both the C-TSF and HTSA algorithms are employed to model the slot. For this case, $w_s = 0.004$ cm, corresponding to $\epsilon_r = 4.6141$, and the equivalent antenna radius a is 0.001 cm for the HTSA. Cubic FDTD cells, 1 cm on a side are used, and the total mesh dimensions are 49 × 49 × 50 cells in the $\hat{x}$, $\hat{y}$, and $\hat{z}$ directions, respectively. The plate is illuminated by a $\hat{z}$-polarized uniform plane wave

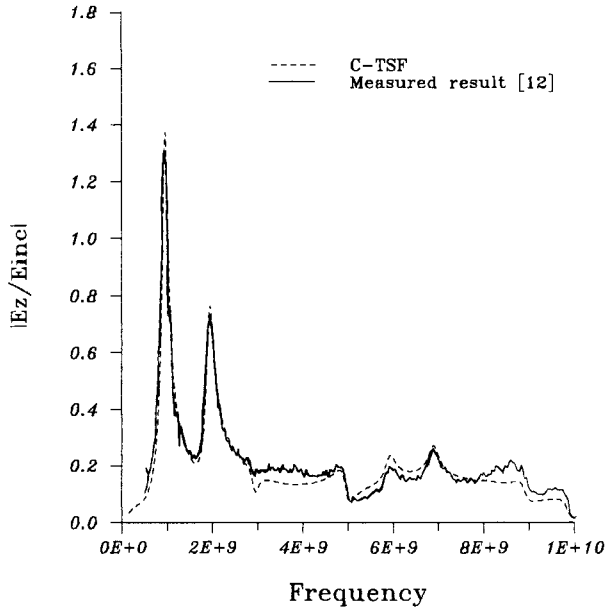

Fig. 6. Comparison between experimental results and the results for a finite-length slot in an infinite conducting plane modeled by C-TSF. The angle of the incident plane wave is $\theta = 60°$.

with a Gaussian-pulse temporal variation given by

$$E_z^{inc}(t) = e^{-(t-t_0)^2/T^2} \tag{9}$$

where $T = 1.214 \times 10^{-10}$ s, and $t_0 = 0.5 \times 10^{-9}$ s. The time step is 16.678 ps. The time delay is chosen to allow the pulse to start with approximately zero amplitude. A total-field/scattered-field formulation is used to implement the source [1]. Second-order Mur ABC's are employed for surface boundary components, and first-order Mur ABC's for boundary edge locations. Single-precision arithmetic is used for this case. The time-domain response for the $\hat{z}$-component of the electric field immediately adjacent to, and centered on the slot for both the C-TSF and HTSA computations is shown in Fig. 8(a). The comparison is in general good, however, there are small phase and amplitude differences. The corresponding frequency-domain response is shown in Fig. 8(b), where a slight difference in the resonance frequency of the slot is apparent.

A loaded rectangular cavity with a single slot is also modeled employing both the C-TSF and HTSA subcellular algorithms for the slot. The cavity dimensions are shown in Fig. 9 [4]. All the relevant FDTD parameters for the mesh dimensions, computational domain, and excitation are the same as those employed for modeling the previous 3-D finite plate. The cavity is loaded by a conducting wire terminated with a 50 Ω resistor at either end. The conducting wire is modeled with a Yee cell by setting the tangential electric field along the wire axis to zero within a Yee cell. The resistors are modeled with a subcellular algorithm reported in [14]. The current induced on the wire at the cavity center is calculated from Ampere's law. Time-domain results are shown in Fig. 10(a), and the magnitude of the Fourier transform is given in Fig. 10(b). The agreement between the two methods is again good. The first, third, fourth, and fifth peaks are cavity

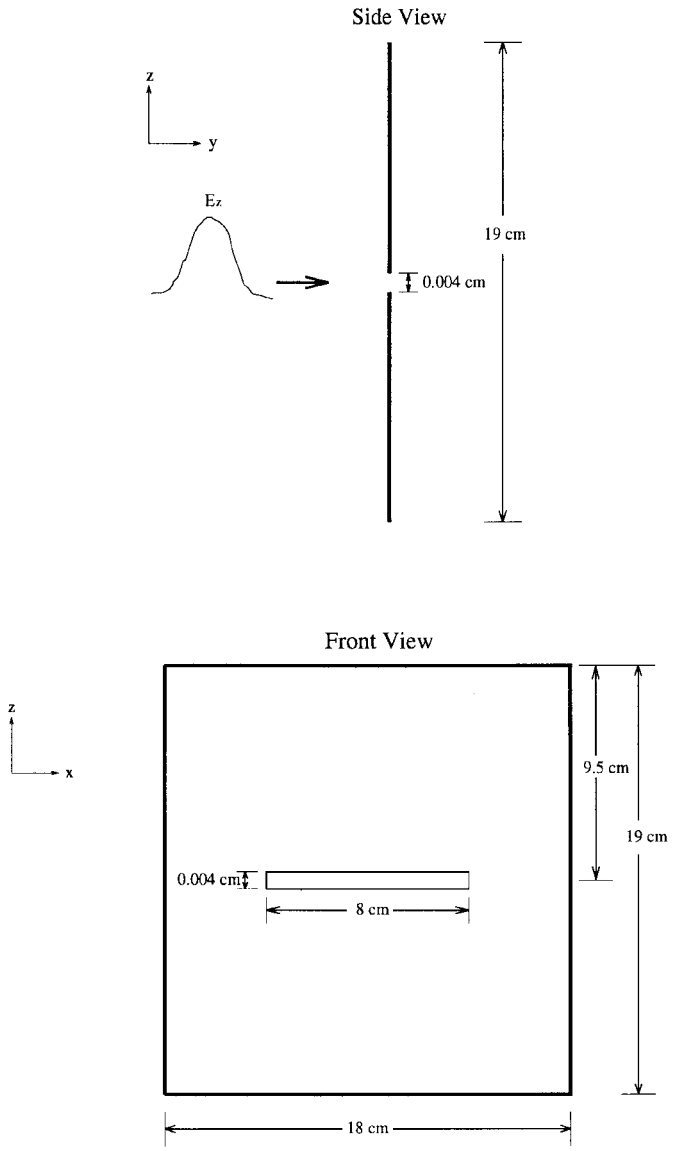

Fig. 7. The geometry of the 3-D finite plate.

resonances. The first null occurring at approximately 1.8 GHz is due to the wire resonance. The second peak is the slot half-wavelength resonance. The discrepancies in amplitude and frequency between the C-TSF and HTSA results for the slot resonance between 1.5 and 1.75 GHz are similar to those of the previous 3-D plate case, as shown in Fig. 8(b).

IV. Enclosure Modeling—FDTD and Measurements

The C-TSF and HTSA algorithms are employed in this section for modeling thin slots in an enclosure, and FDTD results are compared to measurements for power delivered to an enclosure with a slot. The geometry of the experimental conducting enclosure is shown in Fig. 11. The cavity is fed with a 50 Ω coaxial cable probe through a type-N bulkhead connector, which is bonded to the enclosure 360° around its periphery. The center conductor of the probe is extended across the cavity with a 0.16 cm diameter wire, and terminated on the opposite cavity wall with a 1206 package size surface-mount (SMT) 47 Ω resistor soldered to copper tape. The feed

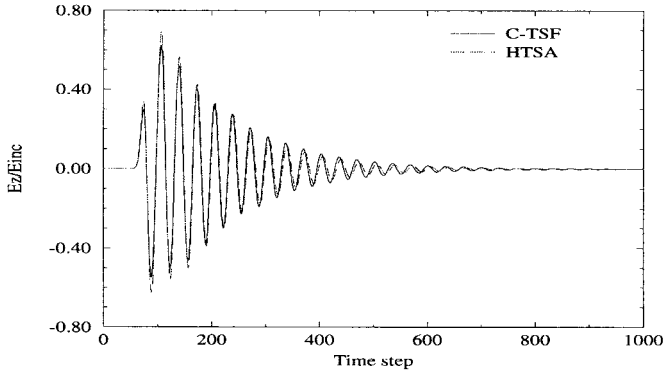

(a)

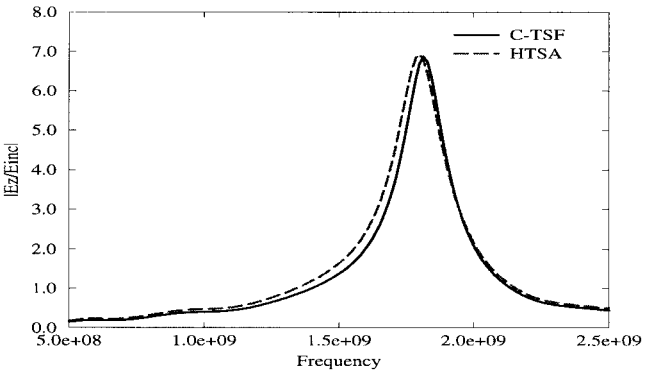

(b)

Fig. 8. E_z sampled in the shadow region immediately adjacent to the slot for (a) time-domain results and (b) FFT results.

is located at $x = 17$ cm, $y = 14$ cm, $z = 15$ cm. The SMT resistor is characterized with an HP4291A Impedance Analyzer, and is a constant $|Z| = 47\ \Omega$ with $|X| < 3\ \Omega$ of reactance over the frequency range of measurement. A Wiltron 37 247A network analyzer is employed to measure the reflection coefficient S_{11}, and the real power delivered by the source is calculated from the 1-port measurements. The power available from the source is 2.5 mW.

The enclosure is constructed of five pieces of 0.635-cm thick aluminum, and one plate of 0.05 cm thick aluminum for the face containing the slot. The slot is located in the face of the termination and 5.5 cm away from the edge of the cavity. The inside dimensions of the enclosure are 22 cm $\times$ 14 cm $\times$ 30 cm. Copper tape with conductive adhesive is used to electromagnetically seal the seams. The frequency range of the measurements is 600 MHz–1.6 GHz in order to excite several cavity modes, slot modes, and the feed-probe TEM mode [13].

The feed probe is modeled by a simple voltage source V_s with 50 Ω resistance incorporated into a single FDTD cell at the feed point. The magnetic fields circling the source are modeled in the same fashion as a thin wire to give the cross-section of the source specified physical dimensions [15]. The resistor is modeled as a lumped element using a subcellular algorithm [14]. The width of the SMT is approximately that of the probe wire diameter, and the physical cross-section dimensions are modeled with the same diameter as that of the probe wire by modifying the magnetic field components circling the SMT in the same fashion as for the source.

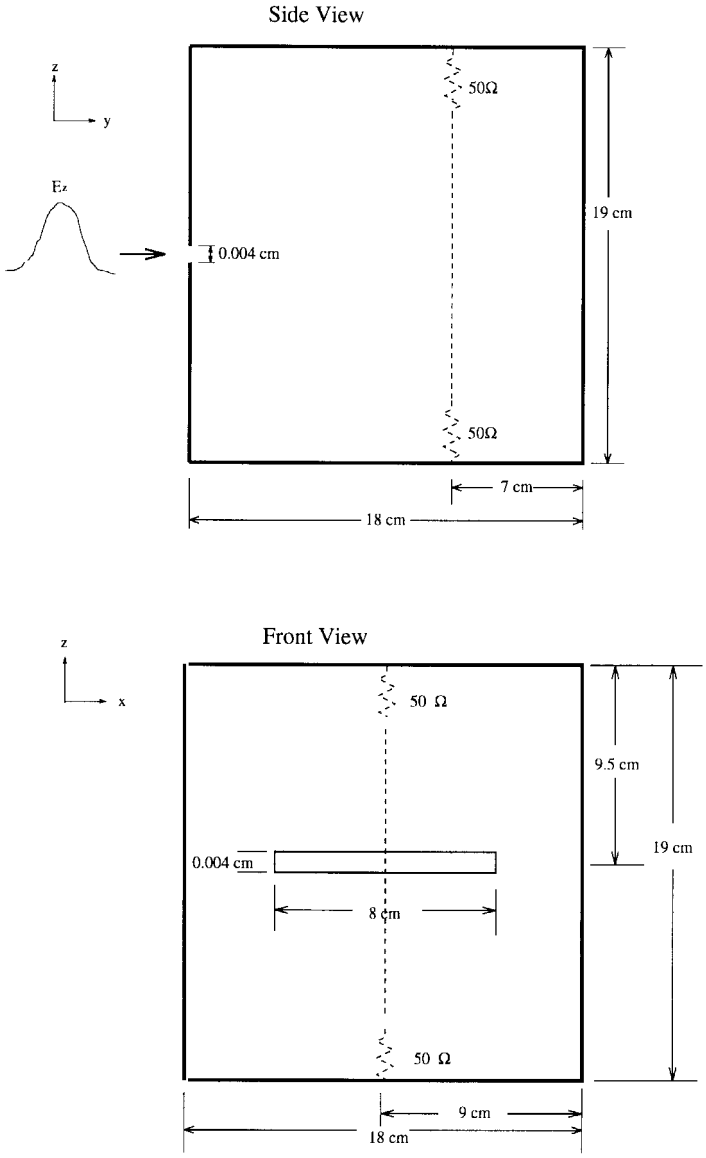

Fig. 9. The geometry of the loaded cavity.

PML absorbing boundary conditions are employed for the 3-D simulations [7].

A sinusoidally modulated pseudo-Gaussian pulse is employed as the excitation. The source voltage as a function of time t is

$$V_s(t) = e^{-\alpha_1^2[f_2-f_1)^2(t-\alpha_2/(f_2-f_1)]^2} \cdot \cos\left[2\pi\,\frac{f_1+f_2}{2}\left(t-\frac{\alpha_2}{f_2-f_1}\right)\right] \qquad (10)$$

where f_1 and f_2 are the designated starting and stopping frequencies of the simulated bandwidth, respectively, and α_1 and α_2 are constants ($\alpha_1 = 1.035$ and $\alpha_2 = 2.539$). This time-variation and constants are chosen for the frequency range from 0.6–1.6 GHz so that the temporal pulse is greater than two orders of magnitude below the maximum at the beginning and end of the pulse. Also the dc component of the transformed signal is greater than five orders of magnitude less than the signal level at the bandwidth boundaries f_1 and f_2. The argument in the modulating cosine is chosen to shift the pulse

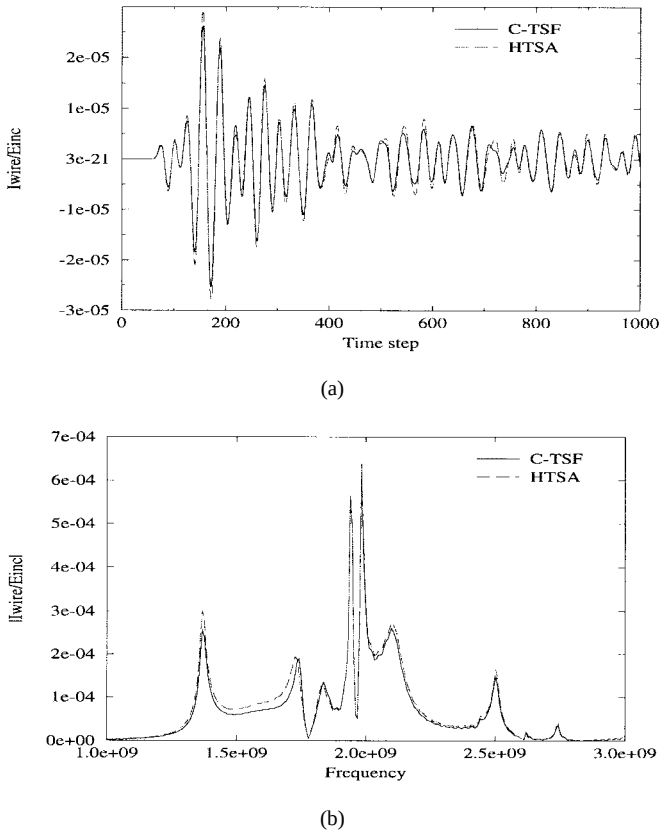

Fig. 10. Time and frequency domain responses for the current induced on the wire in the loaded cavity.

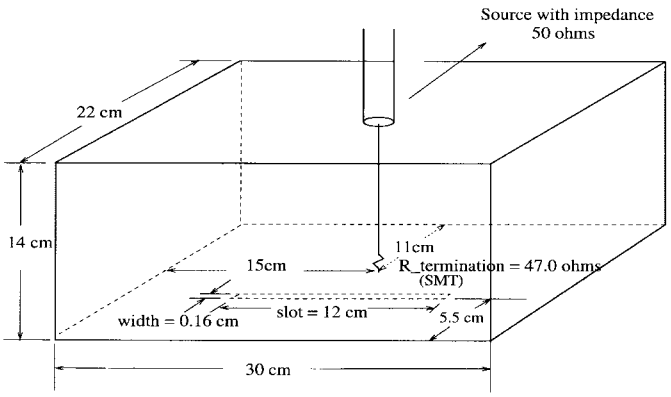

Fig. 11. Shielding enclosure geometry for comparison of FDTD and measured results.

in frequency to the center of the desired bandwidth $(f_1+f_2)/2$. The time-history of the voltage V_0 across the source and source impedance, and the current I_0 through the source are stored, and an FFT is employed to obtain frequency-domain quantities.

A cell size of 1.0 × 0.5 × 1.0 cm and a time step of 8.3333 ps are employed for the C-TSF simulations. Finer discretization along the y-direction is used in order to better model the spatial extent of the SMT load resistor. No instabilities are encountered in the C-TSF simulations.

The HTSA subcellular algorithm for modeling the thin slot is also compared to C-TSF and measurements. HTSA, while more complicated to implement than C-TSF, has the advantage

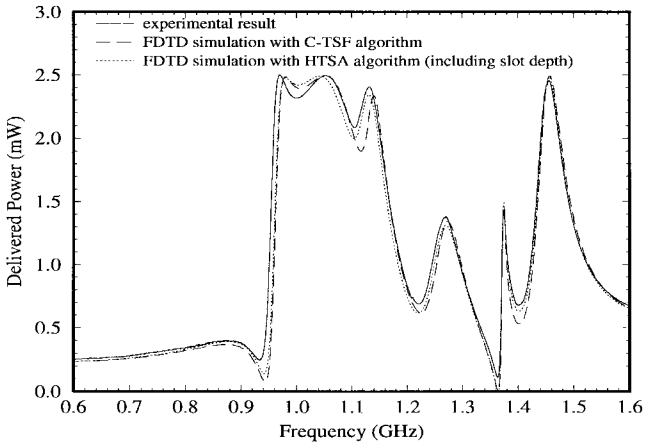

Fig. 12. Comparison of experimental and FDTD results for the configuration in Fig. 11.

that it is inherently 3-D, and the slot depth d is modeled by $a = (w/4)e^{(-\pi d/2w)}$, where a denotes the equivalent antenna radius and w is the slot width [4]. A cell size of 1.0 × 0.5 × 1.0 cm and a time step of 8.3333 ps, as employed in the C-TSF simulations, result in instabilities. The reason is that the subdivision of the HTSA grid for the slot by a factor of two gives a $\Delta = 0.5$ cm along the axis of slot (Δ is the discretization of the slot in HTSA). Thus, the requirement that $\Delta = c \times \Delta t$ in HTSA [4] is not valid for a time step of 8.3333 ps [16]. So a cubic cell of 1 × 1 × 1 cm and time step of 16.6667 ps are employed. Instabilities still occur in the HTSA simulations because the width of the slot ($w_s = 0.1$ cm) is on the order of the spatial step ($\Delta = 0.5$ cm) used in the transient integral equation in HTSA [16]. Before the onset of instability, time can be incremented for 2000 time steps if no slot depth is incorporated, and 3500 time steps if the slot depth of 0.05 cm is incorporated. In the latter case, the equivalent antenna radius is reduced by 39%. The length of the FDTD time histories is extrapolated to 8000 time steps using Prony's method [17].

The results of measurements and simulations for the real power delivered to the enclosure by the source are shown in Fig. 12. The slot depth of 0.05 cm is included in the HTSA simulation. The agreement is generally good. The wall loss is not included in the FDTD simulations and is negligible because the terminating resistor is a much more significant loss mechanism than the wall loss for the configuration investigated [13]. Since the feed-probe wire is along the $\hat{y}$-direction, the $\hat{y}$-component of the electric field is excited, while the $\hat{y}$-component of the magnetic field is suppressed, i.e., only TM_y cavity modes are excited by the probe wire. Resonances at 0.97 and 1.45 GHz correspond to the TM_y101 and TM_y111 modes, respectively. They are 13 and 7% higher than the frequencies of ideal cavity resonances. When the slot is eliminated, both measurements and simulations show that these two cavity resonances are at 0.98 and 1.45 GHz, respectively. The resonance at 1.05 GHz is a result of the terminated feed probe, and corresponds to a TEM mode [13]. The resonances at 1.13, 1.27, and 1.37 GHz are due to the slot because they disappear in both the experiments and simulations when the slot is eliminated.

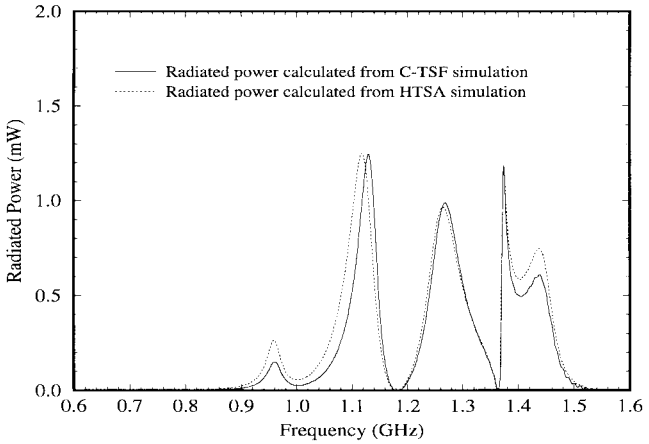

Fig. 13. Comparison of HTSA and C-TSF FDTD simulations for the power radiated through the slot.

The C-TSF and HTSA algorithms result in the same delivered power for the cavity mode resonances TM_y101 and TM_y111 at 0.97 and 1.45 GHz, respectively. The shift of the probe wire TEM mode at 1.05 GHz for the HTSA simulations, compared to the C-TSF simulations and measurements, is caused by the cubic cells employed in the HTSA simulations, which can not well model the spatial extent of the SMT resistor along the y-direction. Employing cubic cells in the C-TSF simulations results in the same shift for the probe wire TEM mode, but no effect for the cavity and slot resonances. At the slot resonances at 1.13 and 1.27 GHz, the simulated result from the HTSA algorithm agrees better with the measurement. The result from the C-TSF algorithm has a small shift to higher frequency of 0.7 and 0.3% at 1.13 and 1.27 GHz, respectively. The power radiated through the slot, shown in Fig. 13, is calculated from the FDTD simulations by subtracting the power dissipated in the load from the power delivered by the source. The results from C-TSF and HTSA simulations agree. The power radiated through the slot is approximately 8, 50, 40, 48, and 25% of the available power at 0.97, 1.13, 1.27, 1.37, and 1.45 GHz, respectively. The C-TSF simulations result in a shift of 1 and 0.4% to higher frequency for the slot resonances at 1.13 and 1.27 GHz, respectively, as compared to the HTSA simulated results. For the slot resonance levels, the C-TSF simulations and HTSA simulations agree well. In the HTSA simulations, the result incorporating zero slot depth shows little discernible difference of resonance frequencies from the result incorporating 0.05 cm modeled slot depth. As a result, the difference in the slot resonance frequencies between the HTSA and C-TSF implementation of the slot is attributed to the former being a 3-D, and the latter a 2-D formulation.

V. Conclusion

Two subcellular thin-slot algorithms are employed with the FDTD method in this study to model an electrically thin slot without refining the mesh in the vicinity of the slot. For plane-wave scattering from a 3-D finite plate and 3-D loaded cavity, both C-TSF and HTSA algorithms yield nearly identical results. Plane-wave scattering from an infinite conducting plane with a finite-length slot is also studied using both C-TSF and HTSA algorithms. For this case, a scattered-field formulation and Liao ABC's are used. Double-precision arithmetic is employed to avoid instabilities associated with the Liao ABC's.

Published measured data is used to study the accuracy of the C-TSF, and the comparison is found to be good up to 5 GHz for the geometry investigated. Beyond 5 GHz, the FDTD cell size is larger than one-twentieth of the wavelength, and this coarse cell resolution is believed to be the cause of discrepancy. The HTSA algorithm produced results very similar to those produced using the C-TSF algorithm. FDTD results employing HTSA and C-TSF for power delivered to and radiated from an enclosure with a thin slot also compare well with measurements. Results for the C-TSF method are presented for slot width to length ratios of $0.0005 < w_s/L_s < 0.013$. The ratio of the slot width to FDTD cell size corresponding to these results is $0.004 < w_s/\Delta\ell < 0.4$ (where $\Delta\ell$ is the FDTD mesh dimension). Over this range, fields outside the slot agree well with either experimental results, or with HTSA results. As a consequence, the C-TSF algorithm is expected to yield reasonably good results over a wide range of w_s/L_s and $w_s/\Delta\ell$.

There are several trade-offs between the C-TSF and HTSA algorithms. The C-TSF algorithm has the advantage that it is straight-forward to implement, and requires only a single computation of an elliptic integral of the first kind above the standard Yee FDTD method. The HTSA approach, by contrast, is significantly more complicated to implement than the C-TSF. A significant advantage of the HTSA algorithm, however, is the ability to model finite-thickness conductors with an equivalent antenna radius. The C-TSF algorithm by contrast is formulated only for conducting planes. This fundamental difference results in a shift of C-TSF predicted half-wavelength resonance frequencies to higher frequency. The shift is only for lower Q resonances ($Q < 20$), and is typically less than 1%. In general, from an EMI perspective this slight shift for slot resonances is not a significant disadvantage. The shift is not so great for the affected Qs that a clock harmonic might occur at a resonance frequency indicated by simulations and not the experimental situation, i.e., predicting a problem where one does not exist. Conversely, the shift is not so great that a problem might occur and not be predicted.

The HTSA algorithm requires several additional multiplications and additions per FDTD cell in modeling a slot than the standard Yee algorithm (with no slot). Additional memory to store the equivalent magnetic currents modeling the slot is required as well. The C-TSF algorithm requires storage for the ϵ_r in the slot, but no additional arithmetic operations over the Yee algorithm (with no slot). In both cases, however, any additional requirements for modeling a slot along one dimension are inconsequential relative to the run time (arithmetic operations) and memory of the overall FDTD algorithm in the 3-D space being modeled. As a practical consequence, differences in computational complexity between the HTSA and C-TSF algorithm for modeling thin slots is not a consideration.

Finally, the stability properties of the HTSA and C-TSF algorithms differ. No instabilities with the C-TSF algorithm have

been encountered in a large number of different simulations employing second-order Mur and PML ABC's [7]. However, the HTSA algorithm is more sensitive and susceptible to instabilities.

ACKNOWLEDGMENT

The authors gratefully acknowledge helpful exchanges with Dr. D. J. Riley, Dr. C. D. Turner, and Dr. L. D. Bacon.

REFERENCES

[1] A. Taflove, *Computational Electrodynamics: The Finite-Difference Time-Domain Method.* Norwood, MA: Artech House, 1995.
[2] K. S. Kunz and R. J. Luebbers, *The Finite Difference Time Domain Method for Electromagnetics.* Boca Raton, FL: CRC, 1993.
[3] J. Gilbert and R. Holland, "Implementation of the thin-slot formalism in the finite-difference EMP code THREDII," *IEEE Trans. Nucl. Sci.*, vol. NS-28, pp. 4269–4274, Dec. 1981.
[4] J. Riley and C. D. Turner, "Hybrid thin-slot algorithm for the analysis of narrow apertures in finite-difference time-domain calculations," *IEEE Trans. Antennas Propagat.*, vol. 38, pp. 1943–1950, Dec. 1990.
[5] G. Mur, "Absorbing boundary conditions for the finite-difference approximation of the time-domain electromagnetic-field equations," *IEEE Trans. Electromag. Compat.*, vol. EMC-23, pp. 377–382, Nov. 1981.
[6] Z. P. Liao, H. L. Wong, B. P. Yang, and Y. F. Yuan, "A transmitting boundary for transient wave analyzes," *Scientia Sinica*, vol. 27, no. 10, pp. 1063–1076, Oct. 1984.
[7] J. P. Berenger, "Perfectly matched layer for the absorption of electromagnetic waves," *J. Comp. Phys.*, vol. 114, pp. 185–200, Oct. 1994.
[8] M. Moghaddam and W. C. Chew, "Stabilizing Liao's absorbing boundary conditions using single-precision arithmetic," in *Proc. 1991 IEEE AP-S Int. Symp.*, London, Ont., Canada, 1991, pp. 430–433.
[9] C. D. Turner and L. D. Bacon, "Evaluation of a thin-slot formalism for finite-difference time-domain electromagnetics codes," *IEEE Trans. Electromag. Compat.*, vol. 30, pp. 523–528, Nov. 1988.
[10] C. M. Butler, Y. Rahmat-Samii, and R. Mittra, "Electromagnetic penetration through apertures in conducting surfaces," *IEEE Trans. Antennas Propagat.*, vol. AP-26, pp. 82–93, Jan. 1978.
[11] C. A. Balanis, *Antenna Theory.* New York: Wiley, 1982, p. 338.
[12] E. K. Reed, and C. M. Butler, "Time-domain electromagnetic penetration through arbitrarily shaped narrow slots in conducting screens," *IEEE Trans. Electromag. Compat.*, vol. 34, pp. 161–172, Aug. 1992.
[13] M. Li, "Investigation of electromagnetic interference through slots in shielding enclosures: Finite-difference time-domain simulations and experiments," M.S. thesis, University of Missouri, Rolla, 1996.
[14] Y. S. Tsuei, A. C. Cangellaris, and J. L. Prince, "Rigorous electromagnetic modeling of chip-to-package (first-level) interconnections," *IEEE Trans. Comp., Hybrids., Manufact. Technol.*, vol. 16, pp. 876–883, Dec. 1993.
[15] D. M. Hockanson, J. L. Drewinak, T. H. Hubing, and T. P. Van Doren, "FDTD modeling of common-mode radiation from cables," *IEEE Trans. Electromag. Compat.*, vol. 38, pp. 376–387, Aug. 1996.
[16] D. J. Riley, private communication.
[17] W. L. Ko and R. Mittra, "A comparison of FD-TD and Prony's methods for analyzing microwave integrated circuits," *IEEE Trans. Microwave Theory Tech.*, vol. 39, pp. 2176–2181, Dec. 1991.

Kuang-Ping Ma was born in Miaoli, Taiwan, R.O.C., in 1967. He received the B.S. degree in aeronautical and aerospace engineering from National Cheng Kung University, Taiwan, in July 1989, the M.S. degree in mechanical engineering from National Taiwan University, Taipei, in July 1991, the M.S. degree in electrical engineering from The University of Missouri, Rolla, in 1993, and is currently pursuing the Ph.D. degree at the University of California, Los Angeles.

From 1991 to 1993, he served in the United States Army as a Second Lieutenant performing research on digital systems and RF transceivers. His main interests include RF transceiver design, VLSI implementation of communication systems, and digital system design.

Min Li was born in China in 1968. She received the B.S. and M.S. degrees (with honors) in physics from the Fudan University, Shanghai, China, in 1990 and 1993, respectively, and the M.S. degree in electrical engineering from the University of Missouri, Rolla, in 1996. She is currently pursuing the Ph.D. degree..

Since 1995, she has studied and worked in the EMC Lab at the University of Missouri, Rolla, and her research and education have been supported by a Dean's Fellowship and an assistantship. Her research interests include numerical and experimental studies of electromagnetic compatibility problems. She is currently involved in shielding enclosure design.

James L. Drewniak (S'85–M'90) received the B.S. (highest honors), M.S., and Ph.D. degrees in electrical engineering from the University of Illinois at Urbana-Champaign, in 1985, 1987, and 1991, respectively.

He joined the Electrical Engineering Department at the University of Missouri-Rolla in 1991 where he is with the Electromagnetic Compatibility Laboratory. His research interests include the development and application of numerical methods for investigating electromagnetic compatibility problems, packaging effects, and antenna analysis, as well as experimental studies in electromagnetic compatibility and antennas.

Todd H. Hubing (S'82–M'82–SM'93) received the B.S.E.E. degree from the Massachusetts Institute of Technology, Cambridge, in 1980, the M.S.E.E. degree from Purdue University, West Lafayette, IN, in 1982, and the Ph.D. degree in electrical engineering from North Carolina State University, Raleigh, in 1988.

From 1982 to 1989, he was employed in the Electromagnetic Compatibility Laboratory, IBM Communications Products Division, Research Triangle Park, NC. He is currently an Associate Professor of Electrical Engineering at the University of Missouri, Rolla. His primary area of research involves the development and application of computational methods for solving problems in electromagnetic compatibility.

Dr. Hubing has earned an Outstanding Teaching award and two awards for faculty excellence. He is the Director of Member Services for the IEEE EMC Society and the Treasurer of the Applied Computational Electromagnetics Society. He also writes the Chapter Chatter column for the IEEE EMC Society newsletter.

Thomas P. Van Doren (S'60–M'69–SM'97) received the B.S., M.S., and Ph.D. degrees from the University of Missouri, Rolla in 1962, 1963, and 1969, respectively.

From 1963 to 1965, he served as an Officer in the United States Army Security Agency. From 1965 to 1967, he was a Microwave Engineer with Collins Radio Company. Since 1967, he has been a member of the electrical engineering faculty at the University of Missouri, Rolla, where he is currently a Professor. His research interests concern developing circuit layout, grounding, and shielding techniques to improve electromagnetic compatibility. He has taught short courses on electromagnetic compatibility to over 10 000 engineers and technicians representing 200 corporations.

Dr. Van Doren received the IEEE EMC Society Richard R. Stoddard Award for his contributions to EMC research and education in 1995. He is a Registered Professional Engineer in the state of Missouri and a member of Eta Kappa Nu, Tau Beta Pi, and Phi Kappa Phi.